Mitigating the Impact of Azimuthal Sampling on the Strength of Radar-Observed Circulations

Feng Nai, Sebastián Torres, and Christopher Curtis

Cooperative Institute for Mesoscale Meteorological Studies, University of Oklahoma, and NOAA/OAR/National Severe Storms Laboratory, Norman, Oklahoma

(Manuscript received 9 September 2019, in final form 26 March 2020)

ABSTRACT

Severe thunderstorms and their associated tornadoes pose significant threats to life and property, and using radar data to accurately measure the rotational velocity of circulations in thunderstorms is essential for appropriate, timely warnings. One key factor in accurately measuring circulation velocity is the azimuthal spacing between radar data points, which is referred to as the azimuthal sampling interval. Previous studies have shown that reducing the azimuthal sampling interval can aid in measuring circulation velocity; however, this comes at the price of increased computational complexity. Thus, choosing the best compromise requires knowledge of the relationship between the radar azimuthal sampling interval and the accuracy of the circulation strength as measured from the radar data. In this work, we use simulations to quantify the impact of azimuthal sampling on the strength of radar-observed circulations and show that the improvements get progressively smaller as the azimuthal sampling interval decreases. Thus, improved characterization of circulations can be achieved without using the finest possible sampling grid. We use real data to validate the results of the simulations, which can be used to inform the selection of an appropriate azimuthal sampling interval that balances the accuracy of the radar-observed circulations and computational complexity.

1. Introduction

Tornadoes are high-impact weather events that threaten lives and property (NOAA 2018). Since the deployment of the Weather Surveillance Radar-1988 Doppler (WSR-88D), National Weather Service (NWS) forecasters have relied on radar-observed signatures that indicate the development and presence of tornadoes to issue warnings to the public (Brotzge and Donner 2013). Two radar signatures that indicate the presence of a tornado are the tornado signature (TS) and the tornadic vortex signature (TVS). Both signatures are typically recognized in Doppler velocity fields by the presence of extreme inbound and outbound velocities that are separated by approximately one radar beamwidth (e.g., Brown et al. 1978; Brown 1998; Brown et al. 2002; Brown and Wood 2012). The velocities corresponding to the maximum inbound and maximum outbound flow of the circulation can be used by NWS forecasters to estimate the rotational velocity, which is an indicator of circulation strength (Brown et al. 1978; Mitchell et al. 1998). The rotational velocity is calculated as

$$V_{\mathrm{rot}} = \frac{|\text{Maximum Inbound Velocity}| + |\text{Maximum Outbound Velocity}|}{2}, \tag{1}$$

and for V_{rot} to accurately measure the true strength of the circulation, the radar-observed velocities must be a faithful representation of the underlying velocity field.

For a given circulation, radar-observed velocities in a TS or TVS are affected by the size and relative location of the radar resolution volumes. In this work, we focus on azimuthal sampling effects. In the azimuthal dimension, the physical size of the resolution volume (referred to as the azimuthal resolution) is determined by the

---

Corresponding author: Feng Nai, feng.nai@noaa.gov

azimuthal beamwidth of the effective antenna radiation pattern (referred to as the effective beamwidth) and the range from the radar (Doviak and Zrnić 2006). The effective antenna radiation pattern is a function of the inherent two-way antenna radiation pattern, the motion of the antenna in the azimuthal direction, the number of samples per dwell, and the data windowing used in signal processing (Torres and Curtis 2007). The relative location of the resolution volume in azimuth is determined by the azimuthal sampling interval (i.e., the spacing between consecutive radials or rays) and the location of the circulation center with respect to the nearest point on the sampling grid.

Radar-observed velocities from resolution volumes that are physically smaller in the azimuthal dimension are more likely to faithfully represent the underlying velocity field. Improving the azimuthal resolution (i.e., reducing the effective beamwidth) can be achieved through a combination of a narrower inherent antenna radiation pattern, a slower antenna rotation rate, fewer samples per dwell, or a more tapered data window. For weather radars, narrowing the inherent two-way antenna radiation pattern requires increasing the size of the antenna, which is not practical. The antenna rotation rate in the azimuthal direction can be slowed at the price of increased volume update time. This is undesirable, especially when observing rapidly evolving phenomena like circulations. Two more practical methods to reduce the effective beamwidth are 1) reducing the number of samples per dwell and 2) using a more tapered data window to weight these samples. However, both of these methods reduce the effective beamwidth at the price of increased variance of all radar-variable estimates (Brown et al. 2002; Torres and Curtis 2007). This trade-off between improved azimuthal resolution and increased variance of estimates has been studied previously and is not the focus of this paper.

Another way to improve the representation of the underlying velocity fields of circulations is by changing the location of the radar resolution volumes in azimuth relative to the location of the circulation. The locations of the resolution volumes are determined by the azimuthal sampling grid, where each grid point is the center of a resolution volume in the azimuth direction. That is, for data collected with a rotating antenna, the azimuth angles of the sampling grid points are used to determine the time series dwells from which corresponding radials of radar variables such as Doppler velocity are obtained (Torres and Curtis 2007). In this manner, dwells of time series data are formed by collecting a given number samples with azimuths centered about each sampling grid point. It is important to

note that for the same effective beamwidth (i.e., the same antenna rotation rate, number of samples per dwell, and data window), we can use sampling grids with different azimuthal sampling spacings. Thus, the azimuthal sampling interval and the effective beamwidth can be controlled independently. In Brown et al. (2002), the authors evaluated the impact of reducing the effective beamwidth of the radar from $\sim 1.4°$ to $\sim 1°$ while simultaneously reducing the azimuthal sampling interval from $1°$ to $0.5°$. The authors concluded that radar variables generated with a $0.5°$ azimuthal sampling interval and a $\sim 1°$ effective beamwidth can lead to improved resolution and detection range of both TS and TVS. Additionally, the authors found that reducing the azimuthal sampling interval to less than $0.5°$ while also reducing the effective beamwidth to less than $1°$ did not lead to significant improvements when detecting TS and TVS. These conclusions were also confirmed by later studies (e.g., Brown et al. 2005; Proud et al. 2009). However, these studies did not investigate the impact of reducing the azimuthal sampling interval while holding the effective beamwidth constant. This will be the focus of this paper.

As mentioned before, the position of the sampling grid with respect to the circulation also affects the accuracy of its measured strength (e.g., Wood and Brown 1997; Brown et al. 2002; Melnikov et al. 2015). Hereafter, the position of the sampling grid with respect to the circulation will be referred to as the sampling-grid relative position. The number of possible sampling-grid relative positions is given by the azimuthal sampling interval divided by the azimuth difference between consecutive transmitted pulses, which is a function of the antenna rotation rate and the pulse repetition time (PRT). That is, dwells can be "shifted" no less than one sample at a time. In Wood and Brown (1997), different sampling-grid relative positions for a $1°$ azimuthal sampling interval were simulated to study the impact on the observed strength of mesocyclones and tornados. Their study showed that sampling-grid positions that contain radials coinciding with the edge of a circulation generated higher V_{rot} compared to sampling-grid positions where radials are offset from the edge of the circulation. This implies that short-term variations in observed circulation strength should not be attributed exclusively to storm evolution since they could also be the result of changes in the relative position of the sampling grid. While it is possible to adjust the sampling-grid positions, it is impossible to determine a priori which sampling-grid position will provide the highest V_{rot} for a given circulation. Because of this, authors of later studies treated the sampling-grid relative position as a random variable in their simulations to account for

all possible scenarios (e.g., Brown et al. 2002; Torres and Curtis 2015).

To mitigate the impact of sampling-grid relative position, Melnikov et al. (2015) proposed to form every possible M-sample dwell by reusing the last $M - 1$ samples from the previous dwell and adding exactly one new sample. This approach reduces the azimuthal sampling interval to the smallest possible value (i.e., the azimuth difference between consecutive transmitted pulses) and thus minimizes the effects of sampling-grid relative positions. While the authors showed the potential of mitigating the impact of sampling-grid relative position by reducing the azimuthal sampling interval, their analysis of the improvement from the fine azimuthal sampling was done using a single case with qualitative comparisons of fields of radar variables. Furthermore, even if optimum, their approach would not be practical for most operational radars due to the larger number of dwells (by at least an order of magnitude) that would need to be processed and distributed.

In this work, we quantify the impacts of reducing the azimuthal sampling interval on the radar-observed strength of circulations. Unlike previous studies, we systematically vary the azimuthal sampling interval while keeping the azimuthal resolution and the variance of radar-variable estimates constant. Our results can be used to inform the selection of an appropriate azimuthal sampling interval that balances the accuracy of the radar-observed circulation and the computational complexity. The rest of the paper is organized as follows. Section 2 describes the simulation methodology and results, section 3 presents two tornado cases observed with different sampling grids, and section 4 concludes with a summary of our findings.

2. Simulations

Simulations were used in previous works to study the impact of the azimuthal resolution (Brown et al. 2002; Proud et al. 2009), the azimuthal sampling interval (Wood and Brown 1997; Brown et al. 2002), and range-oversampling processing (Torres and Curtis 2015) on estimates of V_{rot} from radar-observed circulations. Simulations are also advantageous for our study because they provide access to the underlying velocity field. This allows us to quantify the performance of a given sampling grid by comparing the associated radar-observed V_{rot} with the maximum V_{rot} that can be observed among all sampling grids. Moreover, simulations allow the systematic varying of circulation parameters (i.e., core radius, peak tangential velocity, and range) so that the effects of azimuthal sampling for different circulations
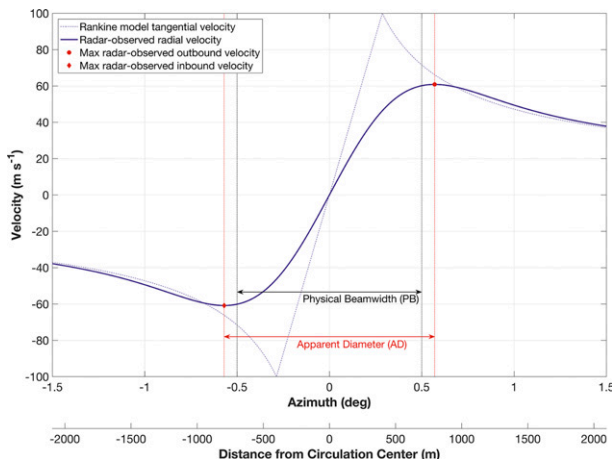

FIG. 1. Model (blue dashed line) and radar-observed (blue solid line) velocities (before sampling) as a function of azimuth for a circulation at a range of 80 km with 100 m s^{-1} peak tangential velocity and 400-m core radius. The radar has a 1° effective beamwidth, which results in a physical beamwidth (PB) of ~1396 m at a range of 80 km. The extrema of the radar-observed velocities (red markers) are used to compute a V_{rot} of 60.9 m s^{-1}, and their locations (vertical red dashed lines) are used to determine an apparent diameter (AD) of ~1592 m. The BADR for this circulation is 0.877.

can be quantified. Our simulation methodology and results are discussed next.

a. Simulation methodology

One approach to simulate radar observations of circulations is to use physically based simulators (e.g., Capsoni and D'Amico 1998; Cheong et al. 2017). These are realistic but highly complex; thus, they are not practical for this study. While not as realistic as their physically based counterparts, simulations based on idealized circulation models have proven to be sufficient to study radar-sampling effects (e.g., Brown et al. 2002; Proud et al. 2009; Wood and Brown 2011; Brown and Wood 2012).

In our simulations, we use the Rankine (1901) combined vortex model to generate the model velocity profile that passes through the center of the circulation at a constant range. This model has the form

$$V(\theta) = V_x (R\tan\theta/R_x)^n \qquad (2)$$

for a circulation at range R and centered at 0° azimuth, where V is the radial velocity at range R and azimuth θ, V_x is the maximum tangential velocity at core radius R_x, $n = 1$ for $R\tan\theta \le R_x$, and $n = -0.6$ for $R\tan\theta > R_x$. Figure 1 shows an example of the model velocity profile (blue dashed line) as a function of azimuth where V_x is 100 m s^{-1}, R_x is 400 m, and the range to the center of the circulation is 80 km. We tested other model velocity

profiles as discussed in Wood and Brown (2011), and their results were similar to results from the Rankine model. However, the improvement to V_{rot} that can be gained via reducing the azimuthal sampling interval was smallest for the Rankine model, which means that the improvements shown in this study are conservative. We made three assumptions on the circulation model: 1) it has constant velocity in range, 2) it has constant velocity in elevation, and 3) it has uniform reflectivity everywhere. While somewhat unrealistic, these assumptions allow us to use simpler simulations. We analyzed the impact of the first assumption in the appendix and found that our conclusions from the simpler model do not change when a circulation model with more realistic variations in range is used. The assumption of constant velocity in elevation was made in numerous studies (e.g., Zrnić and Doviak 1975; Wood and Brown 1997, 2000, 2011; Wood et al. 2001; Brown et al. 2002; Proud et al. 2009; Brown and Wood 2012, 2015; Torres and Curtis 2015) and is supported by numerical simulation results (Wood et al. 2009). Many of the same studies also assume uniform reflectivity.

To calculate the radar-observed velocity profile before sampling, a one-dimensional effective antenna radiation pattern is convolved with the model velocity profile. The effective antenna radiation pattern is assumed to have a Gaussian-shaped main lobe. Similar to previous studies, the sidelobes of the effective antenna radiation pattern are neglected since they are typically tens of dBs below the main lobe peak. In this study, we kept a constant effective beamwidth of 1° because it approximates that of the WSR-88D when collecting superresolution data (Torres and Curtis 2007). The radar-observed velocity profile before sampling is shown in Fig. 1 with a solid blue line. Note that the maximum (red dot) and minimum (red diamond) of the radar-observed velocity profile have the same magnitude due to the symmetry of both the model and the effective antenna radiation pattern. This magnitude is defined as the maximum observable rotational velocity (denoted as V_{rot}^*); that is, it is the maximum V_{rot} that can be observed by the radar for this circulation among all sampling grids when using a 1° effective beamwidth. Note that V_{rot}^* is less than V_x due to the "smoothing effect" of the effective antenna radiation pattern on the model velocity profile. In this case, V_{rot}^* is 60.9 m s^{-1} (recall that V_x is 100 m s^{-1}). In our simulations, estimation noise is not added to the radar-observed velocities because its effects would be the same for all sampling grids, and we are only interested in assessing relative performance across all sampling grids.

In practice, simulations should take into account all possible combinations of circulation radii and distances

from the radar. However, it is possible to reduce the number of circulations that need to be simulated by grouping circulations into families such that, for each member of a family, the impact of azimuthal sampling on the radar-observed strength of circulation is the same. One method to group the circulations into families is to use their beamwidth-to-apparent-diameter ratio (BADR), where the apparent diameter (AD) is defined as the distance between the extrema of the radar-observed velocity profile before sampling. In the example shown in Fig. 1, the physical size of the radar resolution volume in the azimuth dimension [herein referred to as the physical beamwidth (PB)] at a range of 80 km can be computed to be ~1396 m, and the AD is ~1592 m, which results in a BADR of 0.877. Since the PB increases linearly as range increases, circulations that are farther away from the radar must have a larger AD to have the same BADR as circulations that are closer to the radar. For example, circulation A located at 160 km with $V_x = 100$ m s^{-1} and $R_x = 400$ m and circulation B located at 20 km with $V_x = 50$ m s^{-1} and $R_x = 50$ m have the same BADR of 1. The left panel of Fig. 2 shows the radar-observed velocities (before sampling) as a function of azimuth for these two circulations. Note that the extrema (indicated by the dot and diamond markers) of the radar-observed velocity profiles for these two circulations are located at the same azimuths, confirming that the two circulations have the same BADR. The radar-observed velocities before sampling can be expressed as a fraction of V_{rot}^*. This normalization removes the dependency on V_x and allows us to quantify the impact of azimuthal sampling for all cases with the same BADR using a single simulation. The normalized radar-observed velocity profiles for circulations A and B are shown in the right panel of Fig. 2. Since the two normalized curves are identical, the effects of azimuthal sampling for these two circulations are also identical. This implies that results for one circulation with a particular BADR can be generalized to other circulations with the same BADR. In practice, the variance of the velocity estimates for circulations at different ranges could be different because they have different signal-to-noise ratios. However, these differences in the variances of the velocity estimates do not impact our conclusions because they are independent of the sampling grid used and do not affect relative comparisons between different sampling grids.

To evaluate the effects of azimuthal sampling on V_{rot}, we simulated four azimuthal sampling intervals: 1.0°, 0.5°, 0.25°, and 0.125°. For the same relative position, the grids are aligned such that a coarser sampling grid (i.e., one with a larger azimuthal sampling interval) is a subset of a denser one (i.e., one with a smaller azimuthal
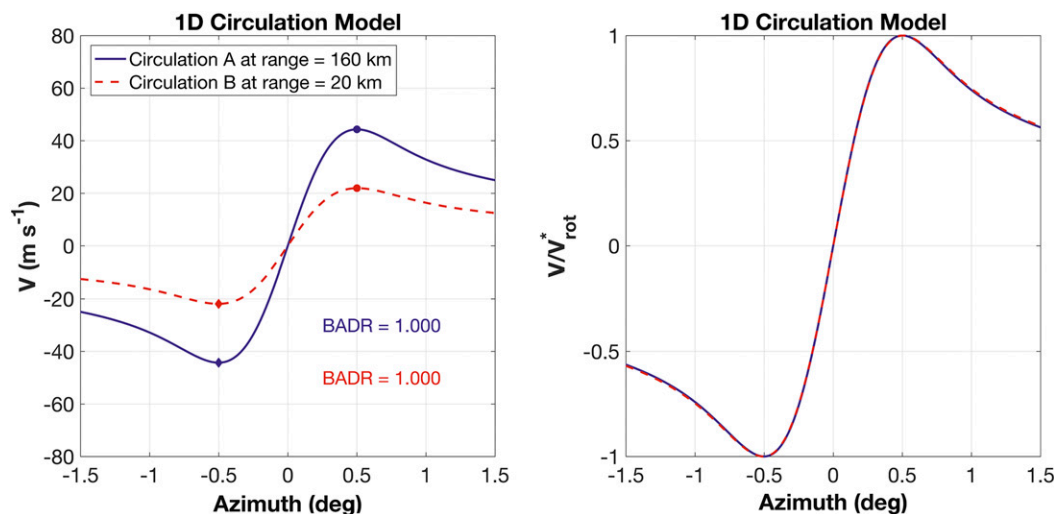
FIG. 2. (left) Radar-observed velocities (before sampling) for circulation A (blue line) and B (red dashed line) for the one-dimensional circulation model. Circulation A is located at 160 km with $V_x = 100 \text{ m s}^{-1}$ and $R_x = 400 \text{ m}$, and circulation B is located at 20 km with $V_x = 50 \text{ m s}^{-1}$ and $R_x = 50 \text{ m}$. Both circulations have the same BADR of 1, and (right) their normalized radar-observed velocities are identical.

sampling interval). That is, a denser sampling grid retains all velocity samples from a coarser sampling grid and provides additional velocity samples at the new grid points. This implies that, compared to a coarser sampling grid, V_{rot} values for a denser sampling grid are always the same or closer to V_{rot}^*. For each circulation, the boundaries of the sampling grid are defined to ensure that the extrema of the radar-observed velocity profile are well within the sampling grid. Without loss of generality, we place the circulation center at 0° azimuth, and initially place the sampling grids such that the center grid point coincides with the center of the circulation. This position of the sampling grid relative to the center of the circulation is referred to as 0° sampling-grid relative position. In general, the sampling-grid relative position is defined as the minimum distance between the center of the circulation (i.e., 0° in our case) and the closest sampling-grid point. To study the effects of different sampling-grid relative positions, the grids are shifted by an azimuth offset varying from −0.5° to 0.5° in 0.005° increments. These offsets span the full range of relative positions for the coarsest sampling grid with a 1.0° azimuthal sampling interval but result in multiple instances of the same sampling-grid relative position for the denser sampling grids (e.g., for a sampling grid with a 0.25° azimuthal sampling interval, azimuth offsets of 0°, ±0.25°, and ±0.5° result in the same sampling-grid relative position of 0°). In other words, the sampling-grid relative position, and consequently V_{rot}, are periodic functions of azimuth offset with period given by the azimuthal sampling interval. However, we apply the same azimuth offsets to all sampling grids (i.e., covering more than one period for the denser grids) to facilitate performance comparisons among different grids.

b. Simulation results

Figure 3 shows an example for circulations with a BADR of 0.833 corresponding to a circulation with $R_x = 400 \text{ m}$ at a range of 68.8 km. The normalized radar-observed velocity profile (solid black line) and velocity samples corresponding to sampling grids with 0.5° (top panel) and 0.25° (bottom panel) azimuthal sampling intervals are shown. When the sampling-grid relative position is 0° (blue dots), reducing the azimuthal sampling interval from 0.5° to 0.25° does not change V_{rot}. Both sampling grids produce a normalized V_{rot} of 0.978. However, when the sampling-grid relative position is 0.125° (red diamonds), the grid with 0.25° azimuthal sampling interval produces a normalized V_{rot} of 0.999 while the grid with a 0.5° azimuthal sampling interval produces a normalized V_{rot} of 0.951. Note that for both relative positions, the grid with a 0.25° azimuthal sampling interval produces normalized values of V_{rot} that are the same or higher than those produced by a grid with a 0.5° azimuthal sampling interval, as expected. This example shows that a change in the relative position of the sampling grid may result in a higher normalized V_{rot} for a denser grid and a lower normalized V_{rot} for a coarser grid.

For each BADR, there is a relationship between the relative position of the sampling grid and the normalized
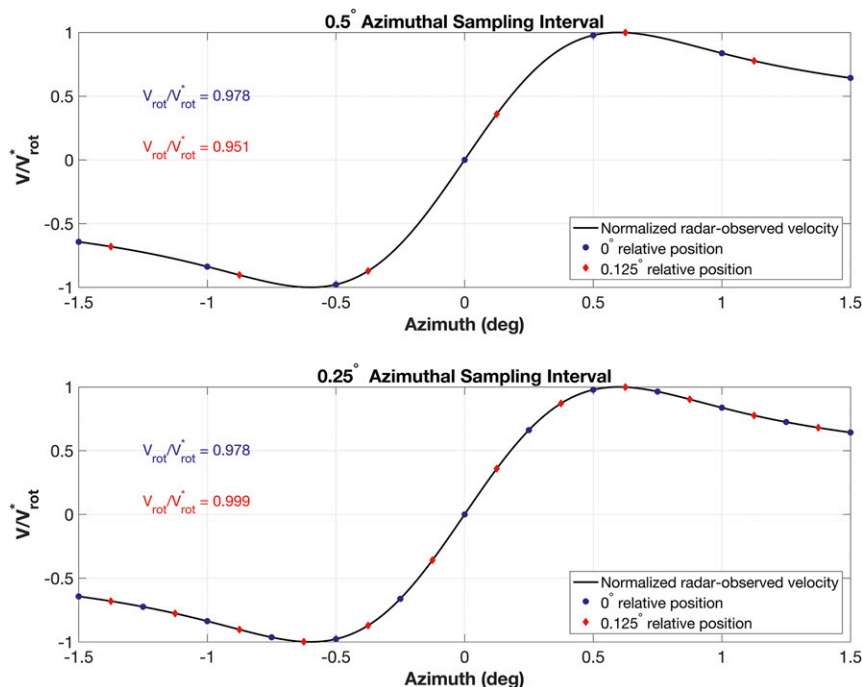
FIG. 3. Normalized radar-observed velocities before sampling (solid black lines) and velocity samples for grids with (top) 0.5° and (bottom) 0.25° azimuthal sampling intervals for a circulation with a BADR of 0.833. Velocity samples for 0° (blue dots) and 0.125° (red diamonds) relative positions are shown for both azimuthal sampling intervals.

V_{rot}; Fig. 4 shows an example of such a relationship for circulations with a BADR of 0.654 corresponding to a circulation with $R_x = 100$ m at a range of 5.2 km. The normalized V_{rot} for grids with 1.0° (black line), 0.5° (blue line), 0.25° (red line), and 0.125° (green line) azimuthal sampling intervals are plotted for different azimuth offsets. As described before, the curves are periodic with period given by the azimuthal sampling interval. Figure 4 also clearly shows that, for a given relative position, reducing the azimuthal sampling interval results in the same or higher normalized V_{rot}. The amount of improvement is largest when the azimuthal sampling interval is reduced from 1.0° to 0.5°, and it gets progressively smaller as the azimuthal sampling interval is further reduced.

In practice, we do not know the sampling-grid relative position; therefore, it makes sense to measure the performance of different sampling grids independent of azimuth offset. For this purpose, we characterize the performance of each sampling grid for a given BADR using the best and worst V_{rot} among all possible relative positions (i.e., the maxima and the minima of curves like the ones in Fig. 4). Better performing sampling grids are those for which the worst-case V_{rot} is closer to V_{rot}^* thus reducing underestimation of radar-observed V_{rot}. From Fig. 4, it is clear that reducing the azimuthal sampling

interval can improve the worst-case V_{rot} (i.e., the minima of each curve increase as the azimuthal sampling interval decreases). Also, the difference between the best and worst V_{rot} decreases for the smaller azimuthal sampling intervals, which means that the sampling-grid
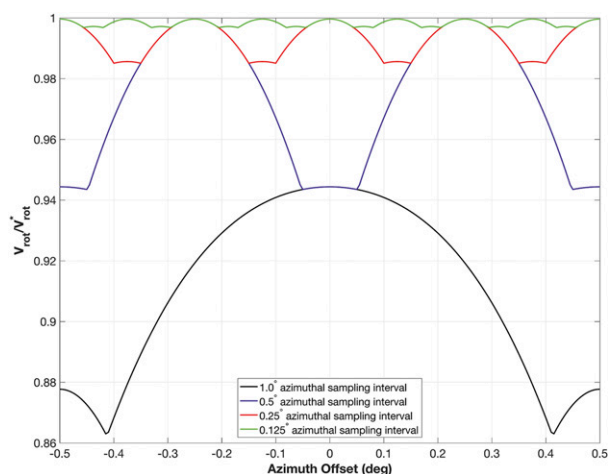

FIG. 4. Normalized V_{rot} as a function of sampling-grid azimuth offset for circulations with a BADR of 0.654. The different curves correspond to sampling grids with azimuthal sampling intervals of 1.0° (black), 0.5° (blue), 0.25° (red), and 0.125° (green).

relative position has less impact on measuring V_{rot}. In turn, this should help to improve the interpretation of radar data because any short-term variations in observed circulation strength can be mostly attributed to storm evolution and not to radar sampling.

The example shown in Fig. 4 demonstrates the advantages of reducing the azimuthal sampling interval for a single BADR. To generalize our results, we conducted a similar analysis for BADRs varying from 0.1 to 1.06. This interval covers a range including large circulations close to the radar (e.g., $R_x = 400$ m and range of 4.6 km) to small circulations far from the radar (e.g., $R_x = 50$ m and range of 114.6 km). Alternatively, for a circulation with $R_x = 50$ m, the BADR interval covers radar ranges varying from 0.6 to 114.6 km. Figure 5 shows the best V_{rot} (solid lines) and worst V_{rot} (dashed lines) for different azimuthal sampling intervals as a function of BADR. It can be seen from this figure that the best V_{rot} (solid line) equals V_{rot}^* only for a few combinations of azimuthal sampling interval and BADR. In all other cases, even the best V_{rot} is underestimated regardless of the sampling-grid relative position. However, for all BADRs, the best and worst V_{rot} get closer to V_{rot}^* as the azimuthal sampling interval is reduced. For grids with azimuthal sampling intervals of 1.0°, 0.5°, 0.25°, and 0.125°, the best normalized V_{rot} values are greater than or equal to 0.917, 0.971, 0.991, and 0.997, respectively, and the worst normalized V_{rot} values are greater than or equal to 0.699, 0.854, 0.956, and 0.990, respectively. This confirms that, for all BADRs, the underestimation of radar-observed V_{rot} is reduced for the finer sampling grids.

Figure 5 also shows that, for all BADRs, the differences between the best and worst V_{rot} for each sampling grid are also reduced when the azimuthal sampling interval is reduced. Among the simulated BADRs, the maximum difference between the best and worst normalized V_{rot} for grids with azimuthal sampling intervals of 1.0°, 0.5°, 0.25°, and 0.125° are 0.298, 0.143, 0.044, and 0.010, respectively. This confirms that reducing the azimuthal sampling interval results in more consistent radar-observed V_{rot} values that are independent of sampling-grid relative positions for all BADRs. Thus, for all circulations, the impact of sampling-grid relative position is reduced when using denser sampling grids. However, the improvements get progressively smaller as the azimuthal sampling interval decreases. That is, reducing the azimuthal sampling interval from 1.0° to 0.5° has the largest improvement while reducing the azimuthal sampling interval from 0.25° to 0.125° has the smallest improvement. Thus, it is not necessary to use the densest sampling grid as proposed by Melnikov et al. (2015) since the majority of the benefits are realized for
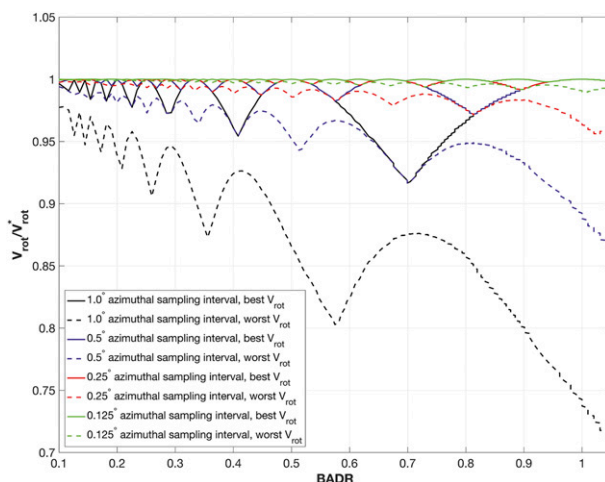

FIG. 5. The best (solid lines) and worst (dashed lines) V_{rot} for each sampling grid among all possible relative positions for different BADRs. The different curves correspond to sampling grids with azimuthal sampling intervals of 1.0° (black), 0.5° (blue), 0.25° (red), and 0.125° (green).

azimuthal sampling intervals on the order of 0.125°. Note that for the sampling grids in our simulations, the computational complexity is doubled as the azimuthal sampling interval is halved (i.e., estimates must be produced for twice the number of sampling grid points). In practice, any increase in computational complexity must be considered when choosing the appropriate sampling grid.

3. Real data

In this section, we corroborate our simulation results using real data. To mimic our simulation experiments, we processed time series (I/Q) data for two cases to produce velocity fields corresponding to different sampling grids using the process described in Torres and Curtis (2007). For each sampling grid, we measured the radar-observed V_{rot} and produced a plot similar to Fig. 4. These data were collected using constant elevation scans where each transmit pulse corresponds to a different azimuth angle, and the azimuth difference between consecutive pulses is given by the product of the antenna rotation rate and the PRT. To generate velocity fields, dwells were formed by taking the returns from the same number of transmit pulses (M) centered in azimuth about each sampling grid point. This process is illustrated in Fig. 6 for $M = 20$ and 3 sampling grids. In this figure, each box on the top axis (labeled as pulses) represents the received I/Q data for all range cells corresponding to a single transmitted pulse. Grids A and B have a 1.0° azimuthal sampling interval while grid C has a 0.5° azimuthal sampling interval. The grid points
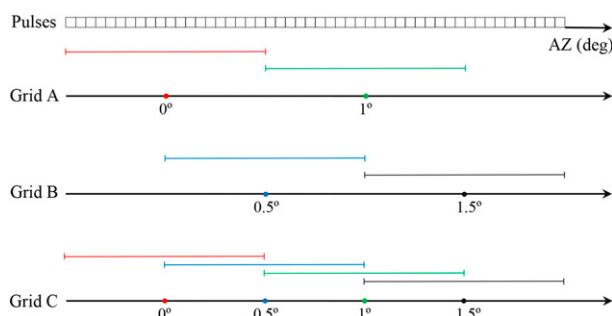
FIG. 6. Illustration of how dwells are formed for different sampling grids. The received I/Q data for all range cells corresponding to a single transmitted pulse are represented by the boxes in the top axis. The grid points are indicated by the colored dots, and the group of pulses used to form the dwell corresponding to a grid point is indicated by the line segment with matching color.

are indicated by the colored dots, and the I/Q data used to form the corresponding dwells are indicated by the line segments with matching colors. Note that because M is kept constant for all sampling grids, adjacent dwells are increasingly overlapped as the sampling grid gets finer (e.g., cf. grid A to grid C in Fig. 6). All dwells were processed using the same data window to maintain a constant effective beamwidth of ~1.0° (and constant azimuthal resolution); this also ensures that the standard deviation of velocity estimates is consistent across different sampling grids. Velocities for each range cell were estimated using the conventional pulse-pair estimator and were manually dealiased and converted to storm-relative velocity to facilitate the measurement of V_{rot}. The dealiasing process consists of three basic steps. First, we identified the general area of the circulation by examining the reflectivity and velocity fields. Next, within this general area, we determined the approximate center of the circulation by looking for the largest azimuthal shear at constant range, which can span two or three range cells depending on the BADR and the sampling grid. Finally, the velocities of neighboring range cells were dealiased using knowledge of the expected wind direction (inbound or outbound) from nonaliased velocities in range gates farther away from the center of the circulation. To introduce the effects of different sampling-grid relative positions, this process was repeated as each sampling grid was progressively shifted in azimuth from −0.5° to 0.5° in 0.02° increments. In the examples shown in Fig. 6, grid A has a 0° azimuth shift, grid B has a 0.5° azimuth shift, and grid C has a 0° azimuth shift (as explained in the previous section, this shift is equivalent to a −0.5° or 0.5° azimuth shift for this azimuthal sampling interval).

The first case we used to corroborate our simulation results is a circulation observed by the KCRI radar located in Norman, Oklahoma, at 2204 UTC 19 May 2013. At the time of observation, the circulation was located at 31.5° in azimuth and 67.6 km in range. Figure 7 shows the storm-relative velocity (SRM) fields of the circulation at 0.5° elevation corresponding to grids with 0° azimuth shift and azimuthal sampling intervals of 1.0° (top-left panel), 0.5° (top-right panel), 0.25° (bottom-left panel), and 0.125° (bottom-right panel). The location and magnitude of the maximum inbound and outbound velocities used to calculate V_{rot} are indicated by the arrows in each panel. The grid with a 1.0° azimuthal sampling interval produced the lowest V_{rot} of 27.0 m s^{-1}, while the grids with 0.5°, 0.25°, and 0.125° azimuthal sampling intervals produced higher values of V_{rot} of 44.45, 50.25, and 50.25 m s^{-1}, respectively. Note that, in this case, reducing the azimuthal sampling interval from 0.25° to 0.125° does not result in higher V_{rot}. This example corroborates our simulation findings: reducing the azimuthal sampling interval can result in the same or higher V_{rot}, and the improvements get progressively smaller as the azimuthal sampling interval decreases.

Figure 8 shows the SRM fields at 0.5° elevation for sampling grids shifted by 0° (left column), 0.16° (center column), and 0.28° (right column), and Table 1 contains the values of V_{rot} for each case. As expected, the relative position of the grid affects V_{rot} (i.e., the values of V_{rot} vary within each row of Table 1). However, the variability reduces as the azimuthal sampling interval gets smaller (i.e., the values of V_{rot} within each row of Table 1 are more consistent as we move from top to bottom). Moreover, for each azimuth shift, denser grids resulted in the same or higher V_{rot} when compared to coarser grids (i.e., V_{rot} is the same or increases as we go down each column of Table 1). These results also corroborate our observations from Fig. 4.

Figure 9 summarizes the results for all sampling grids applied to this case. Similar to what is presented in Fig. 4 using simulations, V_{rot} was computed from velocity fields obtained from the real data and plotted as a function of azimuth shift for grids with different azimuthal sampling intervals. Whereas the manual dealiasing process used so far is quite realistic, it may not be perfect, especially for large BADRs. That is, for weaker or more distant circulations, identifying the approximate location of the center of the circulation can be challenging, and this could lead to velocity dealiasing errors. In turn, any dealiasing errors could result in underestimation of V_{rot}, especially for the coarser grids. When comparing the real-data results with those in Fig. 4, it is important to reduce dealiasing errors because the simulations did not have any aliasing effects. To reduce dealiasing errors for this analysis, we used the velocity field corresponding to the grid with a 0.125°
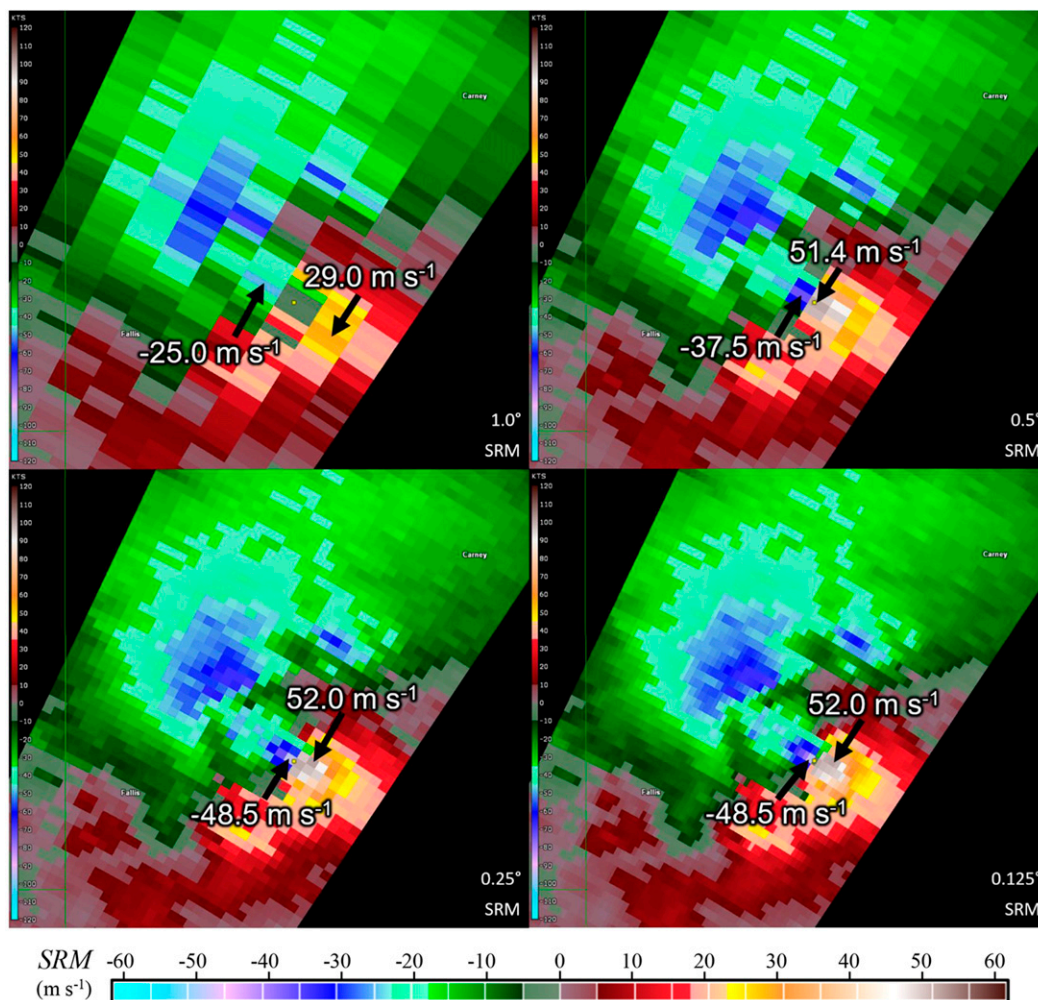
FIG. 7. Storm-relative velocity (SRM) fields at 0.5° elevation for a circulation located at 31.5° azimuth and 67.6-km range observed by the KCRI radar at 2204 UTC 19 May 2013. The same time series data were processed to generate fields corresponding to four sampling grids with 0° azimuth shift and azimuthal sampling intervals of (top left) 1.0°, (top right) 0.5°, (bottom left) 0.25°, and (bottom right) 0.125°. The location and magnitude of the maximum inbound and outbound velocities used to calculate V_{rot} are shown by the arrows.

azimuthal sampling interval with the same azimuth shift to inform the dealiasing of coarser-grid velocity fields. Because we based the dealiasing of the velocity fields corresponding to the coarser grids on the velocity fields corresponding to the grid with a 0.125° azimuthal sampling interval, dealiasing decisions are consistent across the different sampling grids. Thus, relative comparisons of the different grids are not affected by dealiasing errors. Note, however, that this process is not realistic because, in practice, velocity fields on multiple sampling grids would not be available. As a consequence of reducing velocity dealiasing errors, the values of V_{rot} for grids with a 1.0° azimuthal sampling interval are now higher than those listed in Table 1 and are better than what could be achieved if only the 1.0°

azimuthal sampling interval data were used for dealiasing. The curves in Fig. 9 broadly agree with the simulation results in Fig. 4. That is, reducing the azimuthal sampling interval results in the same or higher V_{rot} for the same sampling-grid relative position and in improved consistency when considering all relative positions.

While there is broad agreement between the results from simulations and real data, there are also some noticeable differences. One obvious difference is that the real-data curves shown in Fig. 9 are not symmetrical about 0° azimuth shift because this shift does not correspond to 0° relative position as was the case with the simulations. Additionally, the curves are not symmetrical about their maxima; this could be caused by errors in
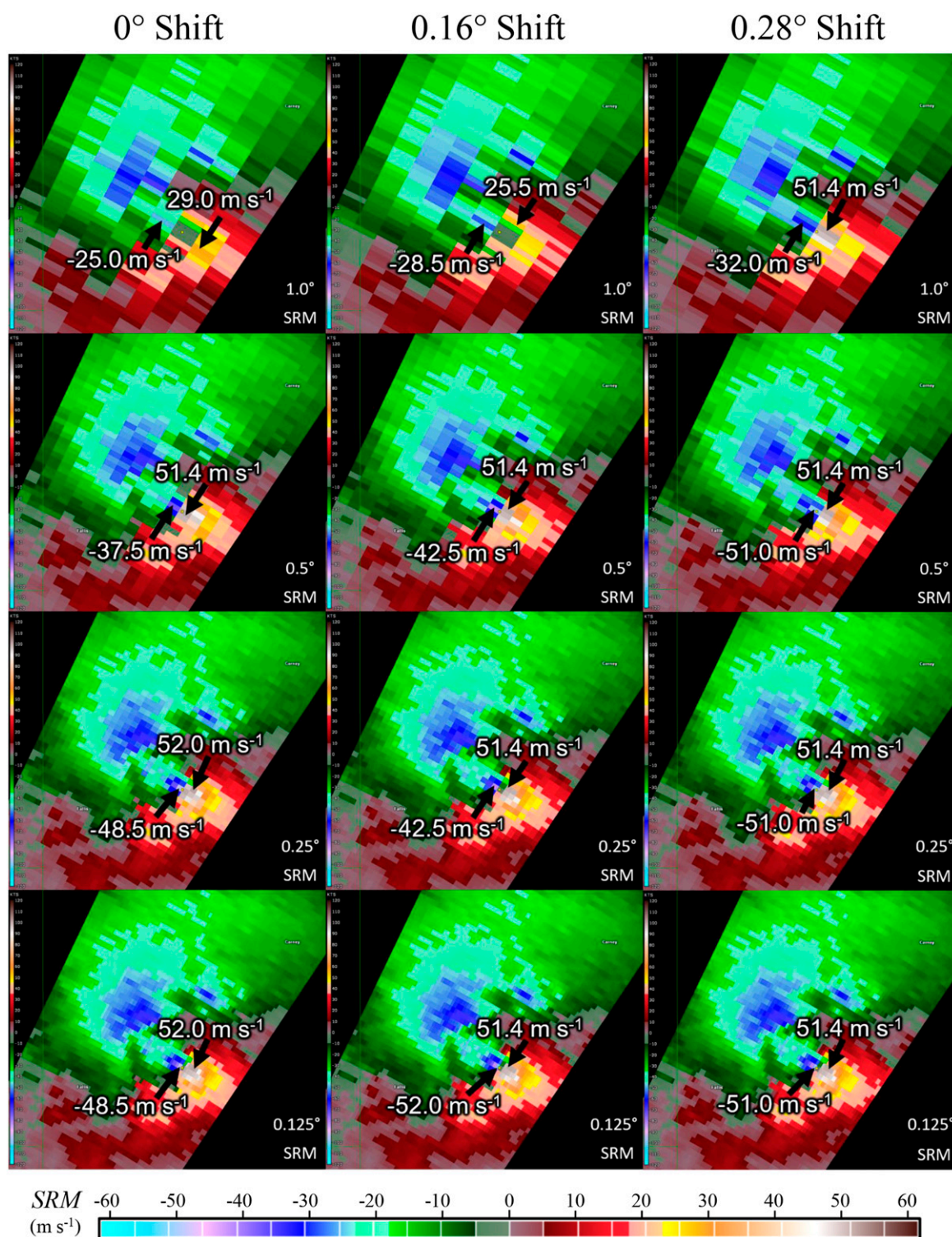
FIG. 8. As in Fig. 7, but for sampling grids shifted by (left) 0°, (center) 0.16°, and (right) 0.28°. The left column repeats the same fields from Fig. 7 for comparison. The values of V_{rot} for each case are listed in Table 1.

TABLE 1. Computed V_{rot} for each case in Fig. 8.

Azimuthal sampling interval (°)	V_{rot} (m s^{-1})		
	0° shift	0.16° shift	0.28° shift
1.0	27.0	27.0	41.7
0.5	44.45	46.95	51.2
0.25	50.25	46.95	51.2
0.125	50.25	51.7	51.2

the estimated storm motion or asymmetry in the circulation itself. Also note that, in the real data, improvement from coarser to denser grids does not follow the same pattern. While the best V_{rot} values for sampling grids with 0.5°, 0.25°, and 0.125° azimuthal sampling intervals are about the same, the worst V_{rot} values do not improve at the same pace as seen with simulations. For example, the minima of the red curve are closer to the minima of the blue curve whereas simulations showed the opposite (i.e., the minima of the red curve were closer to the minima of the green curve). This discrepancy could be caused by statistical errors of velocity estimates. Nevertheless, none of these differences observed in the real-data results change the main conclusion derived from simulation results: reducing the azimuthal sampling interval improves the accuracy of radar-observed circulation strength.

The second case we used to corroborate our simulation results is a circulation observed by the KOUN radar located in Norman at 2105 UTC 9 May 2016. At the time of observation, the circulation was located at 171° azimuth and 75-km range. The same analyses as in the previous case were performed for this case, and the results are shown in Fig. 10. Compared to the previous case, the circulation in this case has a larger BADR since it is a weaker circulation located farther away from the radar. Because of this, identifying the approximate circulation center to perform accurate velocity dealiasing and then compute V_{rot} is more challenging. Despite the curves exhibiting noisier behavior compared to those in Fig. 9, grids with smaller azimuthal sampling interval still result in the same or higher V_{rot} for a given relative position and in improved consistency when considering all relative positions.

4. Conclusions

In this work, we quantified the impact of reducing the azimuthal sampling interval on the radar-observed strength of circulations. Unlike previous studies, we systematically varied the azimuthal sampling interval while keeping the azimuthal resolution and the variance of radar-variable estimates constant. Using simplified simulations, we showed that decreasing the azimuthal
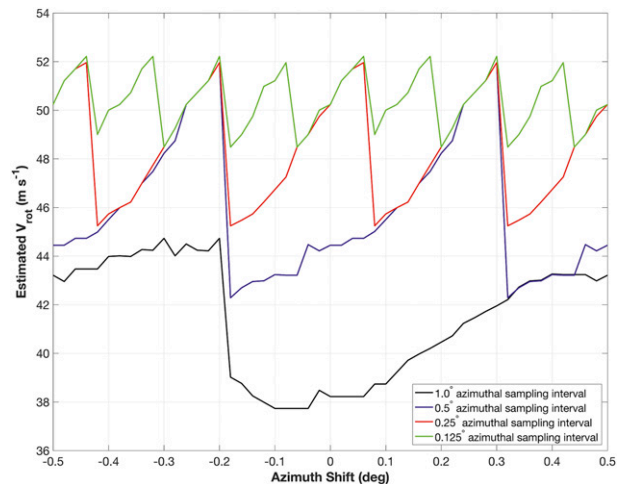

FIG. 9. V_{rot} as a function of azimuth shift for different sampling grids for the circulation observed at 2204 UTC 19 May 2013. The different curves correspond to sampling grids with azimuthal sampling intervals of 1.0° (black), 0.5° (blue), 0.25° (red), and 0.125° (green).

sampling interval leads to a reduction in the underestimation of V_{rot} for all BADRs. Our simulations showed that, for all BADRs, grids with a 0.125° (0.25°) azimuthal sampling interval result in radar-observed circulation strengths that are within 99% (95%) of their theoretical maxima. Moreover, decreasing the azimuthal sampling interval also reduces the impacts of azimuthal sampling for all BADRs. That is, the difference between the best and the worst radar-observed circulation strengths among all sampling-grid relative positions decreases as the azimuthal sampling interval gets smaller.

To corroborate our simulation results, we processed time series data for two circulations and produced
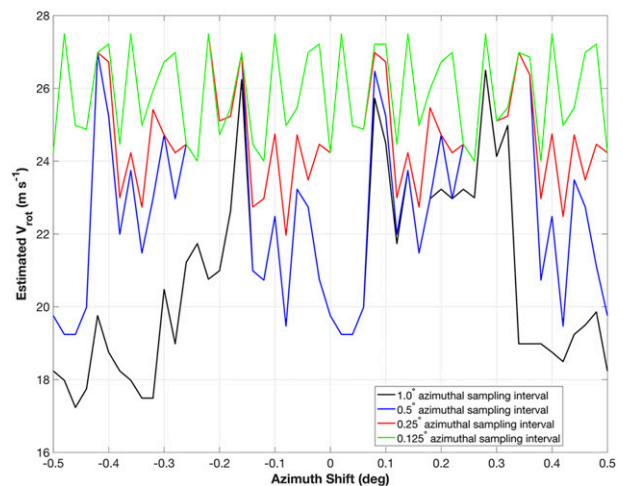

FIG. 10. As in Fig. 9, but for the circulation observed at 2105 UTC 9 May 2016.

velocity fields corresponding to different sampling grids. The variation of V_{rot} as a function of azimuth shift for different sampling grids showed the same features as the simulation results. That is, higher and more consistent radar-observed circulation strengths were measured when using sampling grids with smaller azimuthal sampling interval. Results from simulations and real data also showed that the improvements get progressively smaller as the azimuthal sampling interval decreases, which implies that the majority of the benefits can be realized without using the finest possible sampling grid.

From a practical standpoint, it is important to note that there is a cost associated with using sampling grids with smaller azimuthal sampling intervals. Namely, the use of denser sampling grids leads to more radar data being produced, stored, and transmitted. For example, reducing the azimuthal sampling interval from $0.5°$ to $0.125°$ would quadruple the amount of data. Furthermore, if the volume update times were to remain constant, using denser sampling grids would increase required computational capacity (i.e., the number of computations per second) and transmission bandwidth. These tradeoffs must be taken into account in an operational context, and different ways to address them should be investigated. Solutions will depend on specific hardware and software constraints and end-user needs.

APPENDIX

On the Generality of Using a 1D Circulation Model

In this appendix, we test the robustness of our conclusions with respect to the simplifying assumption that the circulation model has constant velocity in range given by Eq. (1). This simple model is herein referred to as the 1D circulation model. To show that using a circulation model with more realistic variations in range

leads to the same conclusions as using the 1D model, we need to understand the impact of including range effects on the performance of different sampling grids. To do this, we generated a model velocity profile (referred to as the 2D circulation model) that includes range effects by convolving the circulation model used by Torres and Curtis (2015) with a realistic range weighting function (RWF). We used the RWF measured on the KOUN radar: for the 1.57-μs pulse width, it has a 3-dB width of $\sim$250 m.

Before looking at the change in performance for different sampling grids when using the more realistic 2D circulation model, we begin by illustrating the effects using two circulations with different core diameters. The left panel of Fig. A1 shows the radar-observed velocities (before sampling) for circulation A ($R_x = 800$ m) at 88 km and circulation B ($R_x = 100$ m) at 20 km using both the 1D and 2D models. For circulation A (blue and green curves in Fig. A1), the inclusion of range effects results in the same BADR of 0.898 and nearly identical normalized radar-observed velocities (see right panel of Fig. A1). Conversely, the radar-observed velocities for circulation B using the two circulation models are different (cf. the magenta and red curves in the left panel of Fig. A1). Specifically, the BADR changes from 0.99 using the 1D model to 0.898 using the 2D model. Moreover, using the 2D model, the normalized radar-observed velocities (before sampling) for circulations A and B are appreciably different despite having the same BADR (cf. the red and green curves in the right panel of Fig. A1). In summary, when range effects are included, 1) the performance of different sampling grids does not change for circulation A, and 2) despite having the same BADR, there is a small variability in the performance of different sampling grids for circulations A and B. Thus, to generalize our conclusions from Fig. 5, we need to show that our observations based on these examples hold for all BADRs. That is, we need to show that, 1) regardless of the circulation model, the performance of different sampling grids does not change for large circulations, and 2) the performance variability within each BADR family is small enough to not impact our conclusions.

To show that the performance of different sampling grids does not change for large circulations regardless of the circulation model, we compared the performance of different sampling grids using the 1D and 2D circulation models as the range of circulation A varied from 2.5 to 200 km. Fig. A2 shows the maximum absolute differences in normalized V_{rot} among all sampling-grid relative positions when using the two circulation models for all BADRs. The largest maximum absolute differences are 0.0085, 0.004, 0.0015, and 0.0007 for grids
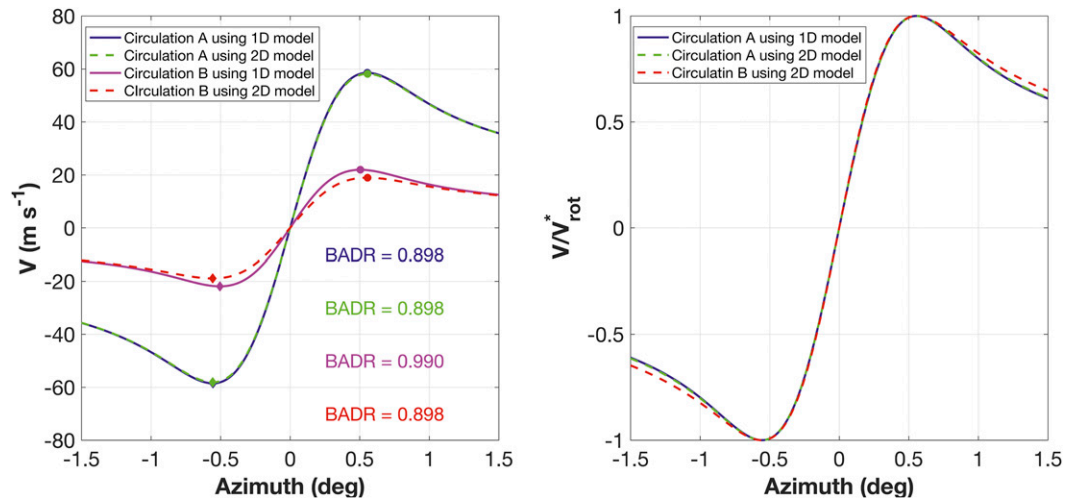
FIG. A1. (left) Radar-observed velocities (before sampling) for circulation A at 88 km and circulation B at 20 km using the 1D (blue and magenta curves) and 2D (green and red curves) circulation models. (right) The normalized radar-observed velocities are nearly identical for the circulations with the same BADR regardless of the model used.

with 1.0°, 0.5°, 0.25°, and 0.125° azimuthal sampling intervals, respectively. These differences are negligible shifts to the curves in Fig. 5 and demonstrate that the performance of different sampling grids is nearly identical at all BADRs for circulation A regardless of the circulation model used. Thus, the results in Fig. 5 immediately generalize to circulations with relative size greater than or equal to that of circulation A, where relative size is defined as the ratio of the circulation diameter to the 3-dB width of the RWF.

To quantify the performance variability within each BADR family, we computed the maximum absolute differences in normalized V_{rot} between circulations A and B when using the 2D circulation model. Circulations A and B were chosen because they represent extreme relative sizes where the 2D model is most likely to cause significant differences in their normalized V_{rot}. Thus, the performance difference between these two circulations provides the upper bound on the performance variability within a BADR family. The BADRs for this analysis were chosen to represent a wide range of realistic scenarios. For example, for a BADR of 0.386, circulation A is located at 20 km and circulation B at 2.91 km, and, for a BADR of 1.016, circulation A is located at 200 km and circulation B at 62.5 km. As shown in Fig. A3, the maximum absolute differences are the largest for grids with a 1.0° azimuthal sampling interval (black curve) with a maximum difference of 0.074 (or 7.4% of V_{rot}^*). For grids with azimuthal sampling intervals of 0.5° (blue curve), 0.25° (green curve), and 0.125° (red curve), the maximum differences are no larger than 0.023 (or 2.3% of V_{rot}^*), 0.0054 (or 0.54% V_{rot}^*), and 0.0016 (or 0.16% V_{rot}^*), respectively. These upper bounds

on the performance variability are smaller than the performance differences between the grids shown in Fig. 5 (recall that differences in performance are quantified by the separation between the dashed lines for a given BADR). This is especially true for large BADRs for which a reduction in the azimuthal sampling interval provides the most benefits.

Based on these results, we show that, 1) regardless of the circulation model, the performance of different sampling grids does not change for large circulations, and 2) the performance variability within each BADR
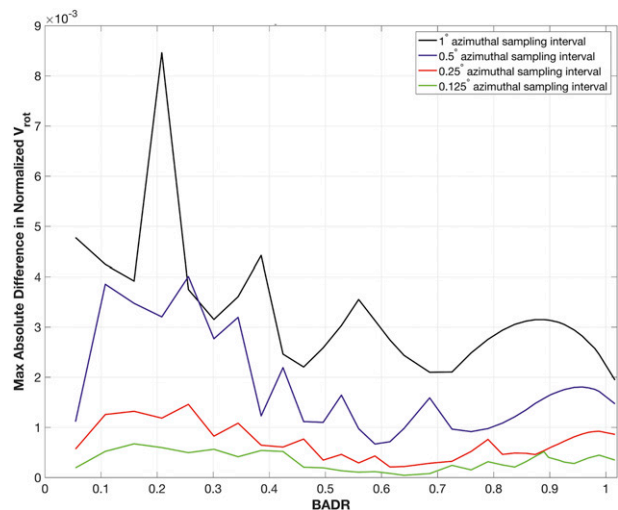

FIG. A2. Maximum absolute differences in normalized V_{rot} between the 1D and 2D circulation models among all sampling-grid relative positions for circulation A. Different curves correspond to grids with azimuthal sampling intervals of 1° (black), 0.5° (blue), 0.25° (red), and 0.125° (green).
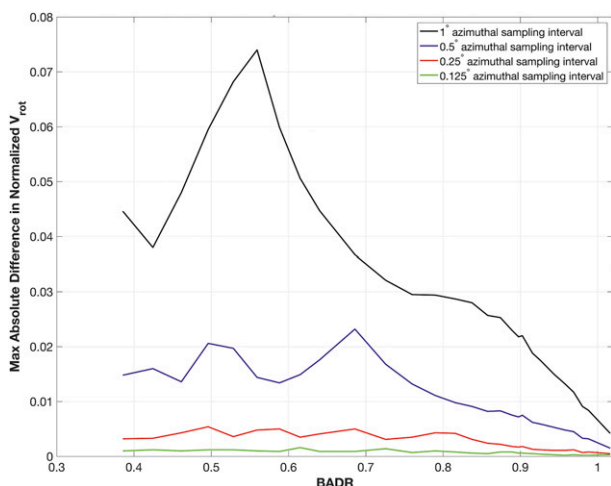
FIG. A3. Maximum absolute differences in normalized V_{rot} between circulations A and B among all sampling-grid relative positions when using the 2D circulation model. Different curves correspond to grids with azimuthal sampling intervals of 1° (black), 0.5° (blue), 0.25° (red), and 0.125° (green).

family is small enough to not impact our conclusions. Therefore, the use of a circulation model with more realistic variations in range is not necessary since it would lead to the same conclusions as when using the simpler 1D model.

REFERENCES

Brotzge, J., and W. Donner, 2013: The tornado warning process: A review of current research, challenges, and opportunities. *Bull. Amer. Meteor. Soc.*, **94**, 1715–1733, https://doi.org/10.1175/BAMS-D-12-00147.1.

Brown, R. A., 1998: Nomogram for aiding the interpretation of tornadic vortex signatures measured by Doppler radar. *Wea. Forecasting*, **13**, 505–512, https://doi.org/10.1175/1520-0434(1998)013<0505:NFATIO>2.0.CO;2.

——, and V. T. Wood, 2012: The tornadic vortex signature: An update. *Wea. Forecasting*, **27**, 525–530, https://doi.org/10.1175/WAF-D-11-00111.1.

——, and ——, 2015: Detection of the presence of tornadoes at the center of mesocyclones using simulated Doppler velocity measurements. *Wea. Forecasting*, **30**, 957–963, https://doi.org/10.1175/WAF-D-15-0014.1.

——, L. R. Lemon, and D. W. Burgess, 1978: Tornado detection by pulsed Doppler radar. *Mon. Wea. Rev.*, **106**, 29–38, https://doi.org/10.1175/1520-0493(1978)106<0029:TDBPDR>2.0.CO;2.

——, V. T. Wood, and D. Sirmans, 2002: Improved tornado detection using simulated and actual WSR-88D data with enhanced resolution. *J. Atmos. Oceanic Technol.*, **19**, 1759–1771, https://doi.org/10.1175/1520-0426(2002)019<1759:ITDUSA>2.0.CO;2.

——, B. A. Flickinger, E. Forren, D. M. Schultz, D. Sirmans, P. L. Spencer, V. T. Wood, and C. L. Ziegler, 2005: Improved detection of severe storms using experimental fine-resolution WSR-88D measurements. *Wea. Forecasting*, **20**, 3–14, https://doi.org/10.1175/WAF832.1.

Capsoni, C., and M. D'Amico, 1998: A physically based radar simulator. *J. Atmos. Oceanic Technol.*, **15**, 593–598, https://doi.org/10.1175/1520-0426(1998)015<0593:APBRS>2.0.CO;2.

Cheong, B. L., D. J. Bodine, C. J. Fulton, S. M. Torres, T. Maruyama, and R. D. Palmer, 2017: SimRadar: A polarimetric radar time-series simulator for tornadic debris studies. *IEEE Trans. Geosci. Remote Sens.*, **55**, 2858–2870, https://doi.org/10.1109/TGRS.2017.2655363.

Doviak, R., and D. S. Zrnić, 2006: *Doppler Radar and Weather Observations*. Dover Publications, 562 pp.

Melnikov, V., D. S. Zrnić, and D. W. Burgess, 2015: Oversampling in azimuth to improve detection of vortices. *37th Conf. on Radar Meteor.*, Norman, OK, Amer. Meteor. Soc., 13B.2, https://ams.confex.com/ams/37RADAR/webprogram/Paper274550.html.

Mitchell, E. D., S. V. Vasiloff, G. J. Stumpf, A. Witt, M. D. Eilts, J. T. Johnson, and K. W. Thomas, 1998: The National Severe Storms Laboratory tornado detection algorithm. *Wea. Forecasting*, **13**, 352–366, https://doi.org/10.1175/1520-0434(1998)013<0352:TNSSLT>2.0.CO;2.

NOAA, 2018: Natural hazard statistics. NWS, https://www.nws.noaa.gov/om/hazstats.shtml.

Proud, J. L., K. K. Droegemeier, V. T. Wood, and R. A. Brown, 2009: Sampling strategies for tornado and mesocyclone detection using dynamically adaptive Doppler radars: A simulation study. *J. Atmos. Oceanic Technol.*, **26**, 492–507, https://doi.org/10.1175/2008JTECHA1087.1.

Rankine, W. J. M., 1901: *A Manual of Applied Mechanics*. 16th ed. Charles Griff and Co., 680 pp.

Torres, S., and C. Curtis, 2007: Initial implementation of super-resolution data on the NEXRAD network. *23rd Int. Conf. on Interactive Information and Processing Systems for Meteorology, Oceanography, and Hydrology*, San Antonio, TX, Amer. Meteor. Soc., 5B.10, https://ams.confex.com/ams/87ANNUAL/techprogram/paper_116240.htm.

——, and ——, 2015: The impact of range-oversampling processing on tornado velocity signatures obtained from WSR-88D superresolution data. *J. Atmos. Oceanic Technol.*, **32**, 1581–1592, https://doi.org/10.1175/JTECH-D-14-00196.1.

Wood, V. T., and R. A. Brown, 1997: Effects of radar sampling on single-Doppler velocity signatures of mesocyclones and tornados. *Wea. Forecasting*, **12**, 928–938, https://doi.org/10.1175/1520-0434(1997)012<0928:EORSOS>2.0.CO;2.

——, and ——, 2000: Oscillations in mesocyclone signature with range owing to azimuthal radar sampling. *J. Atmos. Oceanic Technol.*, **17**, 90–95, https://doi.org/10.1175/1520-0426(2000)017<0090:OIMSWR>2.0.CO;2.

——, and ——, 2011: Simulated tornadic vortex signatures of tornado-like vortices having one- and two-celled structures. *J. Appl. Meteor. Climatol.*, **50**, 2338–2342, https://doi.org/10.1175/JAMC-D-11-0118.1.

——, ——, and D. Sirmans, 2001: Technique for improving detection of WSR-88D mesocyclone signatures by increasing angular sampling. *Wea. Forecasting*, **16**, 177–184, https://doi.org/10.1175/1520-0434(2001)016<0177:TFIDOW>2.0.CO;2.

——, ——, and D. C. Dowell, 2009: Simulated WSR-88D velocity and reflectivity signatures of numerically modeled tornadoes. *J. Atmos. Oceanic Technol.*, **26**, 876–893, https://doi.org/10.1175/2008JTECHA1181.1.

Zrnić, D. S., and R. J. Doviak, 1975: Velocity spectra of vortices scanned with a pulsed-Doppler radar. *J. Appl. Meteor.*, **14**, 1531–1539, https://doi.org/10.1175/1520-0450(1975)014<1531:VSOVSW>2.0.CO;2.